State-Dependent Fragility Curves for Aftershock Seismic Risk Assessment of Japanese Steel Frames

A. Suzuki(1), I. Iervolino(2), M. Kurata(3), S. Shimmoto(4)

(1) Ph.D. candidate, Dipartimento di Strutture per l'Ingegneria e l'Architettura, Università degli Studi di Napoli Federico II, Naples, Italy, akiko.suzuki@unina.it
(2) Full professor, Dipartimento di Strutture per l'Ingegneria e l'Architettura, Università degli Studi di Napoli Federico II, Naples, Italy, iunio.iervolino@unina.it
(3) Associate professor, Disaster Prevention Research Institute, Kyoto University, Kyoto, Japan, kurata.masahiro.5c@kyoto-u.ac.jp
(4) Graduate student, Department of Architecture and Architectural Engineering, Kyoto University, Kyoto, Japan shinmoto.shota.43z@st.kyoto-u.ac.jp

Abstract

Probabilistic seismic risk assessment of civil infrastructures has been attracting attention in Japan, especially after recent mega-earthquakes with a long-lasting series of aftershocks capable of accumulating building damage; e.g., the 2011 Tohoku earthquake. To this aim, it is valuable to be able to assess the failure probability of a particular structure and its evolution in time due to sequential earthquake events, which may cause a difficulty for stakeholders to perform consistent decision making to warrant business continuity. This kind of risk analysis may require state-dependent fragility curves, which in the study were developed for a Japanese steel frame.

To construct the curves, a numerical model of a three-story steel moment-resisting frame was first constructed and calibrated according to the results of shake table tests for a typical Japanese steel structure. This model was subsequently transformed in an equivalent single degree of freedom (ESDOF) system, based on the results of the nonlinear static (pushover) analysis. The probabilistic damage model was then constructed via nonlinear dynamic analysis of the ESDOF system. The spectral acceleration of the elastic period of the ESDOF system was selected as the ground motion intensity measure while the drift angle was selected as response measure. All the records used in the analysis were selected from the Japanese strong-motion network, K-Net. Finally, the state-dependent fragility curves were developed for five levels of damage: *As-New* (AN), *Immediate Occupancy* (IO), *Life Safety* (LS), *Collapse Prevention* (CP) and *Failure* (F). The limit state value for each damage state (DS) was set in compliance with the results of the shake table tests.

After computing the damage state probability due to the mainshock, the time-variant aftershock risk of the steel structure was quantified integrating the developed state-dependent fragility curves with the seismic hazard, following a Markov chain model already available in the literature, which makes use of aftershock probabilistic seismic hazard analysis (APSHA). Hazard was computed assuming that the structure was located in Osaka, a site that may be affected by a mega-earthquake at the Nankai Trough subduction-zone. In particular, in the considered exercise, the most probable damage state due to the considered mainshock scenario was found to be IO, followed, in probability terms, by LS, F, AN, and CP. Given the probability distribution of the mainshock-induced damage, the daily evolution of aftershock damage was computed, and it was found that the most likely DS after two months since the mainshock was still IO followed by F, LS, CP and AN.

Keywords: shake table test; performance-based earthquake engineering; Markovian modeling

1. Introduction

Risk assessment of damaged buildings during aftershock sequences has become relevant recently, as an aid for evacuation, re-occupancy and downtime management decisions. In an emergency, stakeholders, engineers, and building users are challenged by the lack of information regarding the safety of earthquake-affected structures. Especially in weeks/months after an earthquake of large magnitude, a series of aftershocks, which may cumulate damage in buildings, makes such decisions more complicated. For example, more than eight-hundred-fifty aftershocks with magnitude of 5.0 or larger occurred in the following three months in the 2011 Tohoku earthquake [1].

In response to such a demand for post-earthquake decision making, seismic reliability assessment methods have been proposed in the framework of Performance-Based Earthquake Engineering (PBEE) (Cornell and Krawinkler [2]). First, aftershock probabilistic seismic hazard analysis (APSHA) was developed by Yeo and Cornell [3] to quantify the aftershock hazard at a particular site. Furthermore, Luco *et al.* [4] developed a procedure to quantify the residual structural capacity of damaged buildings to withstand repeated earthquakes by considering the structural performance partitioned in a series of damage states (DSs). Then, Iervolino *et al.* [5] proposed a Markov-chain-based solution to provide time-variant seismic reliability by integrating state-dependent fragility curves and APSHA. This approach allows the estimation of failure probability for structures possibly accumulating damage during an aftershock sequence. In this framework, seismic reliability is expressed in terms of transition rates treated as *transition probabilities*; i.e., probabilities that a structure changes its damage state in one time unit (herein day).

To examine the likelihood of damage progress in Japanese buildings during aftershock sequences, this paper presents the state-dependent seismic reliability assessment for a typical Japanese steel frame against a hypothetical aftershock sequence following a mega-earthquake offshore Japan. In fact, the main contribution of the study is the development of the state-dependent fragility curves based on a numerical model calibrated via shake table tests. As a purely illustrative example, APSHA was performed for a site that may be affected by a mainshock at the Nankai Trough subduction-zone, and eventually, the time-variant aftershock risk of the structure was quantified by integrating the developed state-dependent fragility curves and APSHA.

2. State-dependent aftershock reliability analysis of structures

This section briefly recalls the background of state-dependent aftershock reliability analysis of structures according to [5]. This kind of risk assessment requires the definition of a finite number of damage states for a structure, from as-new conditions to structural failure. The time-variant reliability of the structure is expressed by means of a series of matrices, one for each single time unit (i.e., day), which contain the probabilities of the structure traveling from any damage state to any another damage state in the unit time the matrix refers to. In fact, referring to a specific time unit *t*, the matrix is named $\left[P_E\left(t,t+1\right)\right]$. It is a squared matrix $n \times n$, where *n* is the number of damage states, DS_i, $i=\{1,2,\ldots,n\}$ where 1 represents as-new conditions, *n* represents global failure, and $i=\{2,3,\ldots,n-1\}$ represents intermediate damage states.

Each element of the matrix is of the type, $v_{A|m_E}\left(t\right)\cdot P_{i,j}$, where $v_{A|m_E}\left(t\right)$ is the daily rate of aftershocks conditional on the mainshock magnitude, m_E, and $P_{i,j}$ is the probability of transition from DS_i to DS_j, $j>i$, given the occurrence of a seismic event (an aftershock in this case). In summary, $\left[P_E\left(t,t+1\right)\right]$ collects the rate of transition from any damage state to any another in the time unit. These rates are treated as probabilities for small time intervals; see [5] for details.

$$\left[P_E\left(t,t+1\right)\right]=\begin{bmatrix} 1-\sum_{j=2}^{n} v_{A|m_E}\left(t\right)\cdot P_{1,j} & v_{A|m_E}\left(t\right)\cdot P_{1,2} & \cdots & \cdots & v_{A|m_E}\left(t\right)\cdot P_{1,n} \\ 0 & 1-\sum_{j=3}^{n} v_{A|m_E}\left(t\right)\cdot P_{2,j} & \cdots & \cdots & v_{A|m_E}\left(t\right)\cdot P_{2,n} \\ \cdots & \cdots & \cdots & \cdots & \cdots \\ 0 & \cdots & 0 & 1-v_{A|m_E}\left(t\right)\cdot P_{(n-1),n} & v_{A|m_E}\left(t\right)\cdot P_{(n-1),n} \\ 0 & \cdots & \cdots & 0 & 1 \end{bmatrix} \quad (1)$$

The rows and columns of the matrix correspond to the defined damage states, thus, the upper triangle of the matrix refers to transitions from any damage state to any more severe damage state. The diagonal elements are the probability of no damage progress in the time unit (i.e., the rates of seismic events leaving the structure in the same state as it is), and the lower triangle elements are zero because of the irreversibility of damage progress. According to the total probability theorem, the summation of the probabilities in a row is equal to one.

Each element of the matrix of Eq. (1), that is the rate of moving from one damage state to another damage state in a unitary interval, is computed by combining APSHA and structural vulnerability conditional on the occurrence of an earthquake event, *E*. It is precisely given by Eq. (2) which integrates the daily rate of aftershocks conditional on the mainshock magnitude, $\nu_{A|m_E}(t)$, the transition probability from DS_i to DS_j, $P\left[DS_j \mid DS_i \cap IM = im\right], j > i$, conditional on a ground motion intensity measure, *IM*, and the probability density function of *IM* conditional on the occurrence of an aftershock, f_{IM}.

$$\nu_{A|m_E}(t)\cdot P_{i,j} = \nu_{A|m_E}(t)\cdot P\left\lfloor DS_j \mid DS_i \cap E\right\rfloor = \nu_{A|m_E}(t)\cdot \int_{im} P\left\lfloor DS_j \mid DS_i \cap IM = z\right\rfloor \cdot f_{IM}(z)\cdot dz \tag{2}$$

Note that $P\left[DS_j \mid DS_i \cap IM = z\right]$ is derived from the state-dependent fragility curves of the structure in DS_i as in Eq. (3); i.e., subtracting the probability of damage state $j+1$ or worse, conditional on *z* from that of damage state *j* or worse, conditional to the same *IM* value.

$$P\left[DS_j \mid DS_i \cap IM = z\right] = P\left[DS_j\, or\ worse \mid DS_i \cap IM = z\right] - P\left[DS_{j+1}\, or\ worse \mid DS_i \cap IM = z\right] \tag{3}$$

In this framework, the transition matrix for *m* time units, $\left[P_E\left(t, t+m\right)\right]$ is given by Eq. (4); i.e., the product of the matrices referring to the time units of the interval. Finally, the product of the vector collecting the probabilities of the damage states at the beginning of the interval with the resulting probability matrix yields the probabilistic prediction of the damage state at the end of the time interval (to follow).

$$\left[P_E\left(t, t+m\right)\right] = \prod_{i=1}^{m} \left[P_E(t+i-1, t+i)\right] \tag{4}$$

3. Derivation of fragility curves

This section focuses on the development of state-dependent fragility curves for a generic Japanese steel frame, which the adopted method requires in its formulation. To derive state-dependent fragility curves, the study was composed of (1) shake table tests of a scaled specimen, (2) numerical model calibration, and (3) fragility analysis by means of incremental dynamic analysis (IDA [6]).

3.1 Shake table tests of three-story steel frame

A three-story steel moment-resisting frame was selected as the structure of interest in this study, and its seismic performance was examined through the shake table tests of a scaled specimen. Fig. 1a shows the specimen and dimensions. The specimen was originally designed as the reduced model of a full-scale five-story steel frame, and the lowest three-story frame of the original one was extracted for this study (see [7] and [8]). The overall dimensions of the frame are $4{,}000\ \text{mm} \times 1{,}000\ \text{mm} \times 2{,}625\ \text{mm}$; the plan of the frame is two bays by one bay, and beam spans are 2,000 mm along long-side (x) direction and 1,000 mm along short-side (y) direction; the story heights in the vertical (z) direction are 915 mm for the first story and 880 mm for the second and third stories. The long-side is a moment-resisting frame and the short-side is a braced frame. The beams are I-shaped section (I−100×60×6×8) made of SS400 (Japanese Industrial Standards G3101, [9]). The ductile links are inserted at the beam-ends to control flexural strength and deformation capacity of the frame. The columns are also I-shaped section (I−100×100×6×8) made of steel SS400. Additional masses equal to 18.3 kN are put on each floor. Readers can find more details on the frame test bed in [10].

Accelerometers and displacement sensors were installed to examine the structural hysteresis behavior under earthquake excitations. As shown in Fig. 1b, ten accelerometers were put in x direction for each xz structural plane; the measurable range of acceleration was $\pm 2\,\text{g}$ while that of frequency was DC-400 Hz. Also, eight laser-type displacement sensors were installed in x direction for each xz structural plane. The measured responses were filtered through the Butterworth bandpass which passed frequencies between ± 2.5 Hz of the first mode natural frequency for each damage state (the details follow).

The specimen was gradually damaged in x direction by the increasing earthquake loading. The input ground motion (GM) was the JMA Kobe NS wave (1995 Kobe earthquake), provided by the strong ground motion database of Japan Meteorological Agency [11]. In each of the sequential loadings, the amplitude domain of the original wave was scaled by, in order of 14%, 21%,…, 105%, and 112%, i.e., $7\left(k+1\right)\%$, $k=\left\{1,2,\ldots,15\right\}$ where k is the number of the sequential loadings, then followed by 91%, 70%, 49%, and 112%. The time domain was scaled down by the square root of the specimen's scaling factor.

Subjected to the defined sequential loadings, the structure remained elastic until the 21% intensity loading, and the initial yielding initiated at the roof drift approximately equal to 0.4% with the base-shear coefficient equal to 0.5, during the 28% intensity loading. At the 84% intensity loading, the first beam fracture initiated at the second floor, and damage subsequently progressed in some beam-ends. Fractures or cracks were observed at four beam-ends after the 98% intensity loading, while the hysteresis loop during that loading showed that the strength of the frame structure had been increased. At this stage, the structure reached its maximum strength at the roof drift approximately equal to 1.0% with the base-shear coefficient approximately equal to 0.9. The deterioration behavior was observed both in strength and stiffness during the following loadings (105% and 112% of the original waveform), and six beam-ends were found to be damaged at this point. Since then, using the same record, the structure was subjected to a series of lower intensity loadings to represent an arbitrary aftershock sequence; severer damage were then observed, and nine beam-ends were detected as damaged. Finally, the structure was subjected to the 112% intensity loading to trigger near failure. The hysteresis loops obtained in these tests were used as a reference to verify the numerical model (see next section).

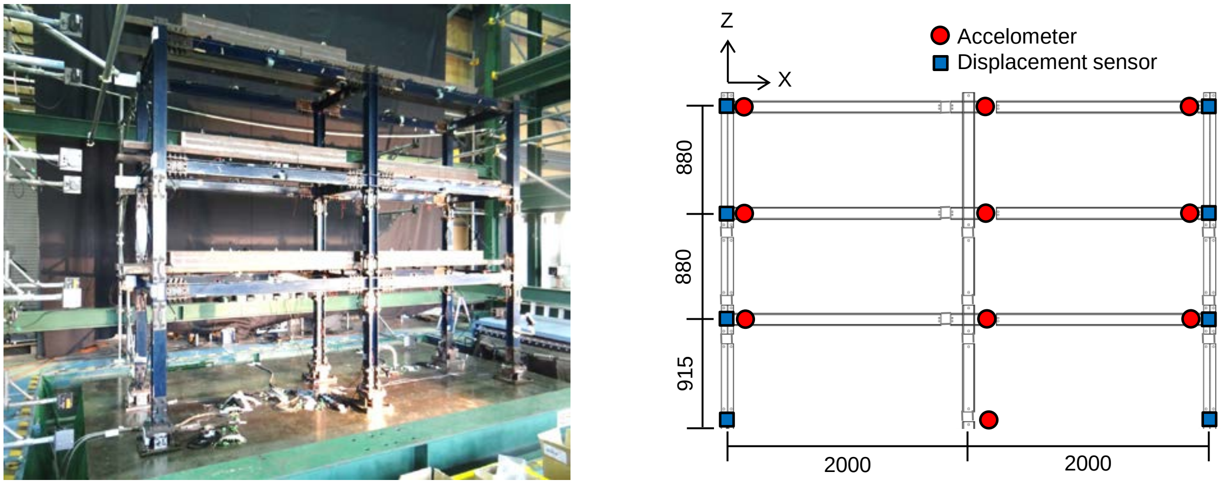

(a) (b)

Fig. 1 – Specimen (unit: mm); (a) picture; (b) dimension and sensor layout.

3.2 Numerical model

The equivalent single degree of freedom (ESDOF) model [12] of the specimen was constructed considering the dissipated energy equivalence and modal contribution. The derivation of the ESDOF model consisted of the following procedure. First, a numerical frame model of the specimen was constructed. The frame model had beam-end plastic hinges whose material properties were determined based on the substructure testing of the beam-end ductile links. The Ibarra-Krawinkler deterioration model [13] was adopted for modeling beam deterioration behavior with local fractures, and the parameters were tuned according to the member's hysteresis loop under cyclic loading (not discussed herein). The pushover (PO) curve of the frame model was obtained from the nonlinear static analysis assuming the force distribution of the first vibration mode. As shown in Fig.

2a, it was observed that the PO curve showed a degree of agreement with the response described in section 3.1, which may be considered satisfactory for the purpose of the study.

Subsequently, the obtained PO curve was converted to the ESDOF model in the form of capacity curve; i.e., base-shear versus deformation. As illustrated in Fig. 2b, the PO curve was idealized as a quadri-linear model consisting of (1) elastic, (2) plastic, (3) deterioration, and (4) residual strength regions, denoted with a dashed line. It was characterized by the following mechanical characteristics: the initial stiffness, *K*, the yield strength, F_y, the yield displacement, D_y, the capping displacement, D_m, and the degrading ratio of the negative stiffness to the initial stiffness, $\beta = K_{det}/K$. Given the identical initial stiffness taken from the PO curve, *K*, the yield strength, F_y, and the capping displacement, D_m, were determined simultaneously, considering the dissipated energy equivalence until intersection of the lines at the yield strength and the original PO curve. The negative stiffness in region (3) was considered identical to the original PO curve and characterized the degrading ratio, β. The constant residual strength, which was derived from the hinge material properties of the frame model, was also accounted for in region (4). Then, the idealized PO curve was further translated to the ESDOF model to account only for the first mode contribution. It was scaled down by the first mode contribution factor, Γ, equal to 1.26 computed from the story masses, m_1, m_2, and m_3. Through the procedure above, all the mechanical properties of the idealized ESDOF model, indicated with asterisks, were derived as summarized in Table 1.

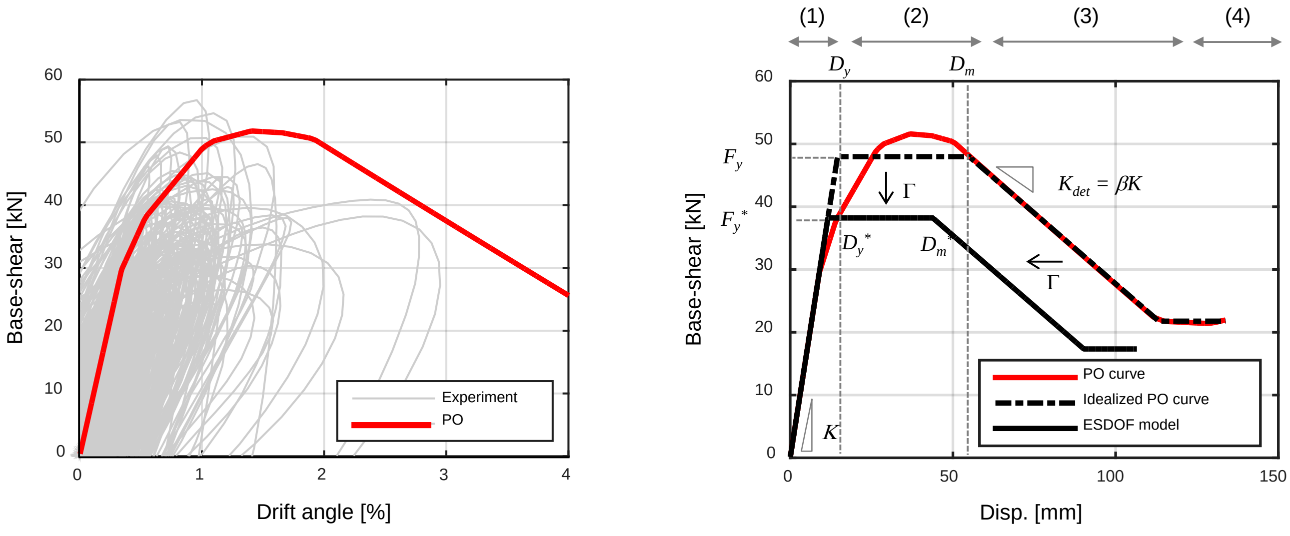

(a) (b)

Fig. 2 – Capacity curves; (a) dynamic responses of the scaled specimen and static PO curve; (b) conversion to ESDOF model.

Table 1 – Conversion to ESDOF model; (top: idealized PO, bottom: idealized ESDOF).

m_1 , m_2 , m_3 [t]	F_y [kN]	D_y [mm]	D_m [mm]	$\beta = K_{det}/K$
1.87	48.0	14.6	55.3	-0.137
m^* [t]	F_y^* [kN]	D_y^* [mm]	D_m^* [mm]	$\beta = K_{det}/K$
3.84	38.3	11.6	44.1	-0.137

The ESDOF model of the scaled specimen was converted into a full-scale model accounting for scaling effect and additional structural weight. Since the examined specimen was the lower three-story frame of the original five-story frame without vertical loads, two and a half times the mass of the full-scale equivalent mass was considered as an additional mass. Table 2 summarizes the parameters for the full-scale ESDOF model with the natural period, T^*, equal to 0.66 sec., the equivalent mass, m^*, and the equivalent height, h^*. The yielding base-shear coefficient was approximately equal to 0.4 while the structural ductility coefficient (up to the capping displacement), D_s, was approximately equal to 0.38. In terms of these structural parameters, the converted model of the structure satisfied the Japanese building code's requirements for steel structures and had a degree of agreement with other full-scale shake table tests [14].

Table 2 – Conversion to full-scale ESDOF model.

T^* [s]	m^* [t]	h^* [mm]	F_y^* [kN]	D_y^* [mm]	D_m^* [mm]	$\beta = K_{det}/K$
0.66	135	7,841	537	43.5	165	-0.137

3.3 Fragility analysis

Using the numerical model, a series of nonlinear dynamic analyses was carried out to derive the state-dependent fragility curves. Prior to the analyses, the five damage states, DS_i, $i = \{1, 2, \ldots, 5\}$, were defined in terms of drift angle, according to the damage observation in the shake table tests. As shown in Table 3, those are *As-New* (AN), *Immediate Occupancy* (OS), *Life Safety* (LS), *Collapse Prevention* (CP), and *Failure* (F): AN represents the elastic branch which ranges from the intact state to yielding at the drift angle equal to 0.5%; IO represents minor yielding without fractures; LS includes the deterioration behavior from the maximum strength; CP represents the structure with many fractures at beam-column connections; F denotes structural global failure.

Table 3 – Damage levels and drift angle limits.

	AN	**IO**	**LS**	**CP**	**F**
Drift angle (%)	0 - 0.5%	0.5% - 1.2%	1.2% - 2.5%	2.5 % - 4.0%	> 4.0 %

3.3.1 Incremental dynamic analysis of the As-New structure

To examine the structural fragility from AN to other damage states, IDA was first conducted using thirty GMs selected from K-Net database [15]: all selected GMs were recorded after the 2011 Tohoku earthquake, the magnitude is in the range of 7.1-9.0. The epicenteral distance is equal to or lower than 400 km; the soil condition of the recording site is categorized as D soil according to the NEHRP scheme [16] (see section 4). The spectral acceleration at the elastic period of the ESDOF, $Sa\left(T^*\right)$, was selected as the *IM*, while the drift angle was taken as response measure. Fig. 3a shows the hysteresis behavior under $Sa\left(T^*\right) = 1.2\,g$. It may be observed that the ESDOF model's hysteresis behavior only includes strength deterioration. Fig. 3b shows the obtained IDA curves and their median. As shown in the first row of Table 4, the median values of the *IM* causing damage state transition are 0.37 g for IO or worse, 0.96 g for LS or worse, 1.59 g for CP or worse, and 1.98 g for F.

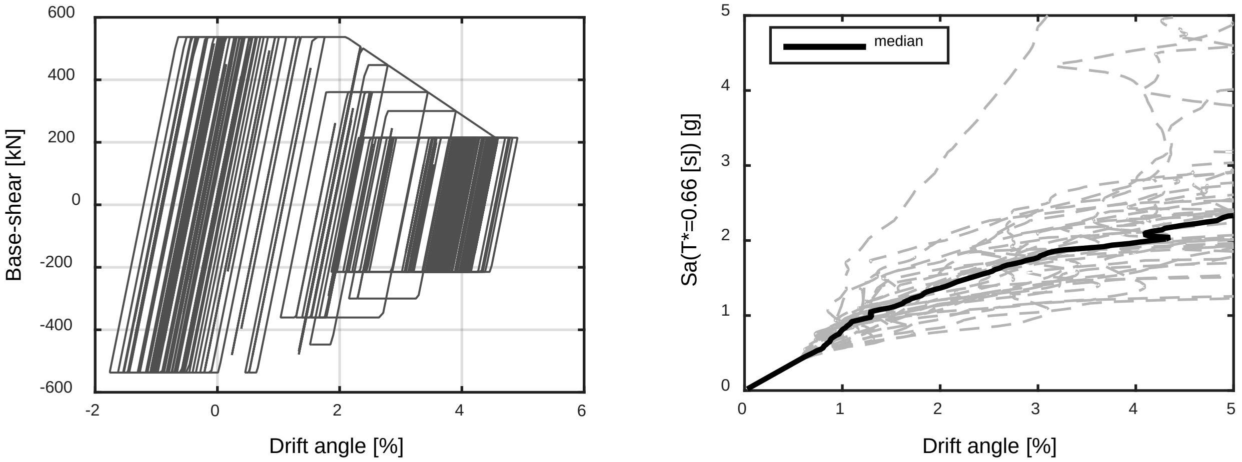

(a) (b)

Fig. 3 – IDA of As-New structure; (a) hysteresis behavior under $Sa\left(T^*\right)=1.2\,\mathrm{g}$; (b) IDA curves.

3.3.2 Back-to-back IDA of the damaged structure

Subsequently, so-called *back-to-back* IDA was performed to examine the fragility of the damaged structure [4]. This analysis involved a series of two successive GMs to realize the damage transitions between one state and a worse one: first, the structure is damaged to the lower bound of DS_i, $i=\{1,2,\ldots 4\}$, with the first GM of the pair of two, then it is further damaged to DS_j, $j=\{2,3,\ldots 5\}$, $j>i$, with the second GM. The minimum spectral accelerations inducing the transition from DS_i to DS_j or worse, $Sa^{i,j}$, were collected for all pairs of GMs considered. For each possible pair of DS_i and DS_j, the median and the logarithmic standard deviation of the sampled $Sa^{i,j}$ accelerations, denoted as $\hat{S}a^{i,j}$ and $\beta^{i,j}$ respectively (the second fifth rows in Table 4), were used as the lognormal fragility parameters. As it might be expected in this analysis, the dynamic capacity of the structure from any DS_i to any DS_j is determined by the residual strength capacity and the residual drift of the structure in DS_i, and the relative margin from that residual drift to the lower bound of DS_j.

Table 4 – Lognormal fragility parameters.

$\hat{S}a^{i,j}$ [g] ($\beta^{i,j}$)	**AN**	**IO**	**LS**	**CP**	**F**
AN	-	3.67E-01 (-)	9.59E-01 (2.38E-01)	1.59E+00 (2.84E-01)	1.98E+00 (3.23E-01)
IO	-	-	9.54E-01 (2.27E-01)	1.57E+00 (2.81E-01)	1.98E+00 (3.13E-01)
LS	-	-	-	1.39E+00 (2.76E-01)	1.91E+00 (3.02E-01)
CP	-	-	-	-	1.53E+00 (3.30E-01)

Compared to the median spectral acceleration to cause failure starting from As-New conditions (i.e., AN to F), the median spectral acceleration to cause the transition between IO and F damage states was the same, and this is because there is no residual drift before yielding at the lower bound of the IO damage state. Then, the median spectral acceleration to cause failure when the structure was in LS damage state was reduced by 4% with respect to that from AN to F. At this point, before the initiation of the strength deterioration, the residual drift (0.4% median) was the only contribution to that reduction. For the structure in CP damage state, the median spectral acceleration to cause failure F was further reduced by 23% with respect to that from AN to F. The sudden reduction in the median capacity here was driven by the softening of the structure. As it regards the logarithmic standard deviations, they increase moving horizontally in each row of the table.

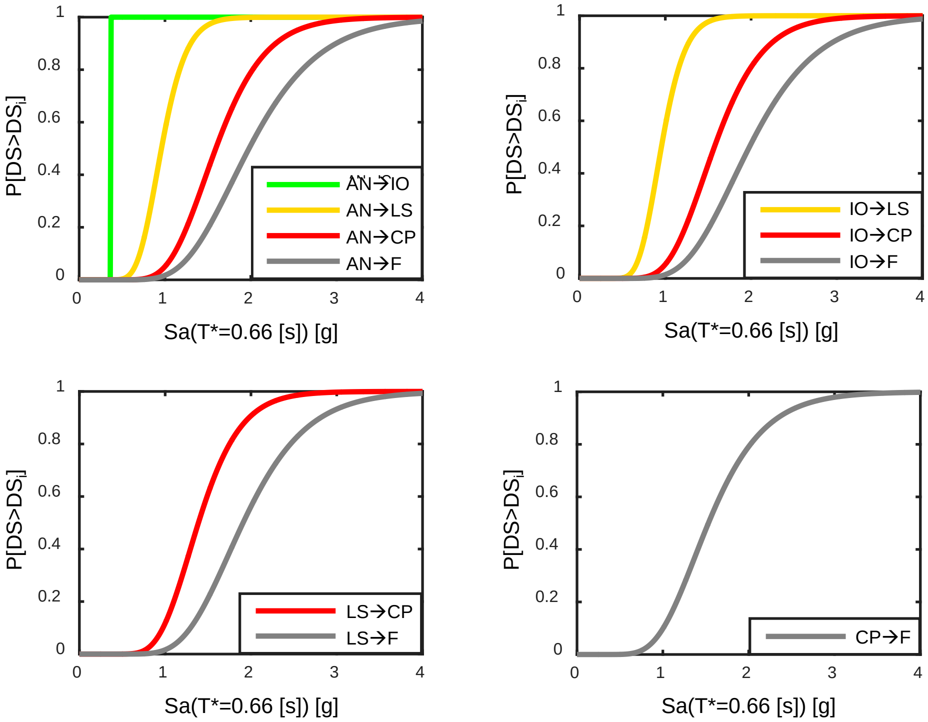

Fig. 4 – State dependent fragility curves.

Note that there are slight discrepancies in fragility parameters between the first and second rows (for the structure starting from AN and from IO, respectively) although those are expected to be identical to each other if exactly following the methodology in [4]. The minor differences (statistically insignificant), are due to slight implementation differences between IDA and back-to-back IDA. With the parameters in the table, state-dependent fragility curves were derived assuming lognormal models, as shown in Fig. 4.

4. Time-variant aftershock risk

In this section, the time-variant aftershock risk of the structure was quantified integrating the presented state-dependent fragility curves with the seismic hazard, following the Markov chain model proposed in [5].

4.1 APSHA for the case-study site

In APSHA, the daily rate of *IM* exceedance at the structure's site, $\lambda_{im}\left(t\right)$, is given by Eq. (5), where it combines the daily aftershock rate conditional on the mainshock magnitude, $v_{A|m_E}\left(t\right)$,the *IM* exceedance probability conditional on the magnitude and source-to-site distance of aftershocks, as respectively denoted as M_A and R_A, $P\left[IM > z \mid M_A = x, R_A = y\right]$, from a ground motion prediction equation (GMPE), and the probability density function of magnitude and source-to-site distance of aftershocks conditional on the mainshock magnitude (m_E), and distance (r_E, location in fact), $f_{M_A,R_A|m_E,r_E}$.

$$\lambda_{im}(t) = \nu_{A|m_E}(t) \cdot \int_r \int_m P\left[IM > z \mid M_A = x, R_A = y\right] \cdot f_{M_A,R_A|m_E,r_E}(x,y) \cdot dx \cdot dy \tag{5}$$

APSHA was performed for the Osaka site, which may be affected by a mega-earthquake with moment magnitude of $m_E = 9.0$ at the Nankai Trough subduction-zone. The considered soil class is D. To this aim, the daily aftershock rate was calculated via Eq. (6), where the lower and upper bounds of magnitude were $m_{A,min} = 7.0$ and $m_{A,max} = 9.0$, respectively.

$$\nu_{A|m_E}(t) = \left(10^{a+b(m_{A,max}-m_{A,min})} - 10^a\right) \Big/ (t+c)^p \tag{6}$$

Coefficients *a* and *b* are the parameters of a *Gutenberg-Richter (GR) relationship* [17], while *c* and *p* are those of the *Modified Omori-law* [18]. These coefficients were set according to the study referring to the aftershock sequence of the 2003 Miyagi-Ken-Oki earthquake [19]. The *GR relationship* for the defined range of aftershock magnitude has $b = 0.931$ [20]. To derive the distribution of the selected seismic *IM*, the Uchiyama & Midorikawa's GMPE [21] was considered.

The probability density function of the source-to-site distance of aftershocks was derived considering that an aftershock could occur in the whole Nankai Trough (and only there), as shown in Fig. 5a. It is as a subduction-zone caused by the subduction of the Philippine Sea plate beneath the Eurasian continental plate, which is the expected source for the mainshock [22]. For the purposes of this study, the original source area has been idealized as rectangle; the width and length are 658 km and 190 km, respectively; this area was divided into 66×19 cells so that each cell is $10 \text{ km} \times 10 \text{ km}$ in size. The focal depth was considered to be at the plate boundary depth between Eurasian continental plate and Philippine Sea plate. The plate boundary depth in the assumed source area varies from 0 km to 60 km. The uniform distribution of aftershock locations was assumed in the area, and then the source-to-site distance was computed from the epicentral distance and the focal depth at each point in the source area. The resulting probability distribution of *IM* exceedance in one aftershock event at the site, $f_{IM}(z)$, is denoted as the dashed line in Fig. 5b. The solid line in Fig. 5b is the *IM* distribution at the site due to a selected mainshock scenario, to be discussed in the next section.

4.2 An illustrative example for a mainshock-affected structure

As a purely illustrative example, the time-variant aftershock risk assessment for the structure was explored using the obtained fragility curves and APSHA just described. To get the time-variant probability matrices for the aftershock sequence described in Eq. (1), the transition probabilities between DS_i to DS_j, $j > i$, given an

(a) (b)

Fig. 5 – APSHA results; (a) site and source zone; (b) the probability distribution of *IM* exceedance in one aftershock event, f_{IM}, and the probability distribution of *IM* exceedance for the mainshock of given magnitude and source-to-site distance, $f_{IM|M_E,R_E}$.

aftershock occurrence, $P_{i,j}$, were derived through the integration of the obtained fragility curves and the hazard for an aftershock event, as indicated in Eq. (2). Table 5 shows the resulting matrix given aftershock occurrence.

Table 5 – Transition probabilities given aftershock occurrence, $P_{i,j}$.

$P_{i,j}$	**AN**	**IO**	**LS**	**CP**	**F**
AN	9.33E-01	4.88E-02	1.11E-02	2.49E-03	4.82E-03
IO	0	9.82E-01	1.10E-02	2.72E-03	4.76E-03
LS	0	0	9.90E-01	4.47E-03	5.09E-03
CP	0	0	0	9.92E-01	8.30E-03
F	0	0	0	0	1

Subsequently, a probability vector was introduced to provide the probabilities that the considered mainshock scenario produced a certain damage, which was initial to the aftershock sequence. To this aim, the probability distribution of *IM* exceedance for the mainshock of given magnitude and source-to-site distance, $f_{IM|M_E,R_E}$, was derived considering the selected GMPE (extrapolated) for a mainshock with magnitude of 9.0 and source-to-site distance equal to 99 km (Fig. 5b). Using Eq. (7), the probability vector of damage state at time $t=0$ that is the time of the mainshock, $\left[P_E(0)\right]$, was obtained, and it is reported in Eq. (8). It may be observed that it is most likely, in this mainshock scenario, that the damage state is IO, probabilistically followed by LS, F, AN, and CP.

$$P_{DS_j} = \int_{im} P\left[DS_j \mid AN \cap IM = z\right] \cdot f_{IM|M_E,R_E}\left(z\right) \cdot dz \tag{7}$$

$$\left[P_E(0)\right] = \left[P_{AN}\left(0\right) \quad P_{IO}\left(0\right) \quad P_{LS}\left(0\right) \quad P_{CP}\left(0\right) \quad P_F\left(0\right)\right] = \left[0.114 \quad 0.381 \quad 0.224 \quad 0.075 \quad 0.206\right] \tag{8}$$

Under these assumptions, the probability distribution of damage state as a function of discrete time units *t*, $t=\{1,2,\ldots,60\}$, is illustrated in Fig. 6. The probability vector of the damage state at each time, $\left[P_E\left(t\right)\right]$, is given by the product of the given initial probability vector in Eq. (8) and the product of transition matrices for each time unit until *t*:

$$\left[P_E\left(t\right)\right] = \left[P_E\left(0\right)\right] \cdot \prod_{i=1}^{t} \left[P_E\left(i-1,i\right)\right] \tag{9}$$

As an example, the computed vector of damage state probabilities two months after the mainshock (i.e., at $t=60$) is shown in Eq. (10). Its elements correspond to the probabilities at sixtieth day from Fig. 6. It is most likely for the structure to stay in IO damage state still sixty days after the mainshock. However, the probabilities of other states changes with respect to the instant after the mainshock. In fact, the second most probable DS is F, followed by the probability of the structure in LS, CP and AN in descending order of probability; see [23] for further discussions.

$$\left[P_E\left(60\right)\right] = \left[P_E\left(0\right)\right] \cdot \prod_{i=1}^{60} \left[P_E\left(i-1,i\right)\right] = \left[0.046 \quad 0.340 \quad 0.258 \quad 0.096 \quad 0.260\right] \tag{10}$$

The purely illustrative value of these numbers has to be, however, recalled. It is mostly due to the simplifications and assumptions about the source of aftershocks and the parameters of the aftershock rate equation in APSHA, as well as the considered mainshock scenario.

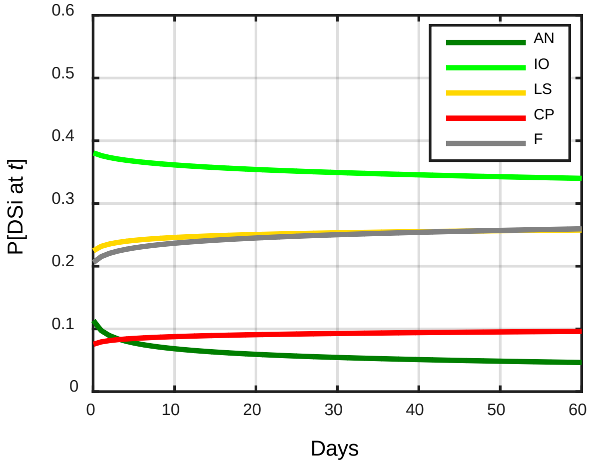

Fig. 6 – Transition probability of structural damage state as a function of time *t* given the initial damage probability vector due to M 9.0 mainshock at 99 km in distance.

5. Conclusions

The seismic performance of a three-story moment-resisting frame was examined through the collapse test of a scaled specimen. A numerical frame model was constructed based on the examination of the deterioration behavior at the component level. Then, state-dependent fragility curves were derived. The resulting curves were integrated with illustrative aftershock probabilistic seismic hazard analysis. The time-variant transition probabilities between damage states were quantified following a time-variant seismic reliability assessment method using Markov chains. The main conclusions of this case study are:

1. in the test, until the structure reached its maximum strength, beam damage, such as fracture or cracks, was detected at four beam-ends in the frame specimen; it was subsequently observed that the strength of the frame structure had been increased (hardening) even with local fractures; after the initiation of strength deterioration, severer damage were induced by a sequence of lower amplitude input;
2. compared with the median capacity of the structure in AN state, the median spectral acceleration to cause failure did not change much until LS, yet it suddenly dropped by 23% if the initial damage state was CP; the reduction was triggered by the structural softening;
3. particular for the assumed mainshock scenario considered, the case study showed that the order of the most probable damage state due to the mainshock was IO followed by LS, F, AN, and CP; given the probability distribution of the mainshock-induced damage, it was most likely for the structure to stay in IO damage state two months after the mainshock day; however, the order of the most probable damage state, except IO, two months after the mainshock day changed from that due to the mainshock.

Finally, it is to mention that study represents an example of experimental approaches to construct a probabilistic structural damage model, although further examinations are required to discuss the consistency of modeling and shake table tests and its impact on the reliability modeling.

Acknowledgements

The authors gratefully acknowledge the funding support offered by the General Collaborative Research program of the Disaster Prevention Research Institute, Kyoto University under Project Number 26G-08 (PI: Iunio Iervolino). Also, this research was achieved using strong-motion records from K-Net, NIED.

References

[1] Japan Meteorological Agency, http://www.data.jma.go.jp/svd/eqev/data/2011_03_11_tohoku/index.html (last accessed April, 2016).

[2] Cornell CA, Krawinkler H (2000): Progress and challenges in seismic performance assessment. *PEER Center News*, **3**(2), 1-3.

[3] Yeo GL, Cornell CA (2009): A probabilistic framework for quantification of aftershock ground-motion hazard in California: methodology and parametric study. *Earthquake Engng Struct.l Dyn.*, **38**(1), 45–60.

[4] Luco N, Bazzurro P, Cornell CA (2004): Dynamic versus static computation of the residual capacity of mainshock-damaged building to withstand an aftershock. In the proceedings of the *13th World Conference on Earthquake Engineering, 13WCEE*, Vancouver, Canada.

[5] Iervolino I, Giorgio M, Chioccarelli E (2016): Markovian modeling of seismic damage accumulation. *Earthquake Engng Struct. Dyn.*, **45**(3), 441-461.

[6] Vamvatsikos D, Cornell CA (2002): Incremental dynamic analysis. *Earthquake Engng Struct. Dyn.*, **31**(3), 491-514.

[7] Kurata M, Li X, Fujita K, Yamaguchi M. (2013): Piezoelectric dynamic strain monitoring for detecting local seismic damage in steel buildings. *Smart Mater. Struct.*, **22**(11), 115002.

[8] Hatakeyama N, Matsushima S, Kawase H (2014): A study on identification of the physical parameters of a full-scale steel structure based on observed record. *J. Struct. Constr. Eng.*, AIJ, **79**(701), 905-912 (in Japanese).

[9] Japan Industrial Standards, http://www.jsa.or.jp/default_english/default_english.html (last accessed April, 2016).

[10] Nishino H, Suzuki A, Masahiro K, Nakashima M (2015): Residual seismic performance evaluation of earthquake-affected steel frames based on local damage detection and model updating, *J. Constr. Steel*, JSSC, **23** (in Japanese).

[11] Japan Meteorological Agency, http://www.data.jma.go.jp/svd/eqev/data/kyoshin/jishin/hyogo_nanbu/index.html (last accessed April, 2016).

[12] Fajfar P (2000): A nonlinear analysis method for performance-based seismic design. *Earthq. Spectra*, **16**(3), 573-592.

[13] Lignos D, Krawinkler H (2011): Deterioration modeling of steel components in support of collapse prediction of steel moment frames under earthquake loading*. J. Struct. Eng.*, ASCE, **137**(11), 1291-1302.

[14] Lignos D, Hikino T, Matsuoka Y, Nakashima M (2013): Collapse assessment of steel moment frames based on E-Defense full-scale shake table collapse tests. *J. Struct. Eng.*, **139**(1), 120-32.

[15] National research Institute for Earthquake science and Disaster prevention, strong motion seismograph networks (K-Net), http://www.kyoshin.bosai.go.jp/ (last accessed April, 2016).

[16] Allen TI, Wald DJ (2009): On the use of high-resolution topographic data as a proxy for seismic site conditions (VS30). *Bull. Seism. Soc. Am.*, **99**(2A), 935-943.

[17] Gutenberg B, Richter F (1956): Magnitude and energy of earthquakes. *Annals of Geophysics*, **9**(1), 1-15.

[18] Utsu T, Ogata Y (1995): The centenary of the Omori formula for a decay law of aftershock activity. *J. Phys. Earth*, **43**(1), 1-33.

[19] Ogata Y, Katsura K (2006): Immediate and updated forecasting of aftershock hazard. *Geophys. Res. Lett.*, **33**(10).

[20] Nanjo K, Sakai S, Kato A, Tsuruoka H, Hirata N (2013): Time-dependent earthquake probability calculations for southern Kanto after the 2011 M9.0 Tohoku earthquake. *Geophys. J. Int.*, **193**(2), 914-919.

[21] Uchiyama Y, Midorikawa S (2006): Attenuation relationship for response spectrum on engineering bedrock considering effect of focal depth. *J. Struct. Constr. Eng.*, AIJ, **606**, 81-88 (in Japanese).

[22] Headquarters of Earthquake Research Promotion (2013): Long term evaluation of seismic activity at Nunki trough (in Japanese)

[23] Suzuki A, Kurata M (adviser) (2016): Data-driven assessment of residual seismic performance and aftershock risk of earthquake-affected structures. Master thesis at Kyoto University.